Linearly polarized excitation enhances signals from fluorescent voltage indicators

Bloxham, William; Brinks, Daan; Kheifets, Simon; Cohen, Adam E.

DOI
10.1016/j.bpj.2021.10.028

Publication date
2021

Document Version
Final published version

Published in
Biophysical Journal

Biophysical Journal
Article

Biophysical Society

Linearly polarized excitation enhances signals from fluorescent voltage indicators

William Bloxham,[1,2,3] Daan Brinks,[1,4,5] Simon Kheifets,[1] and Adam E. Cohen[1,2,*]
[1]Department of Chemistry and Chemical Biology and [2]Department of Physics, Harvard University, Cambridge, Massachusetts; [3]Physics of Living Systems, Department of Physics, Massachusetts Institute of Technology, Cambridge, Massachusetts; [4]Department of Imaging Physics, Delft University of Technology, Delft, the Netherlands; and [5]Department of Molecular Genetics, Erasmus University Medical Center, Rotterdam, the Netherlands

ABSTRACT Voltage imaging in cells requires high-speed recording of small fluorescent signals, often leading to low signal/noise ratios. Because voltage indicators are membrane bound, their orientations are partially constrained by the plane of the membrane. We explored whether tuning the linear polarization of excitation light could enhance voltage indicator fluorescence. We tested a panel of dye- and protein-based voltage indicators in mammalian cells. The dye BeRST1 showed a 73% increase in brightness between the least and most favorable polarizations. The protein-based reporter ASAP1 showed a 22% increase in brightness, and QuasAr3 showed a 14% increase in brightness. In very thin neurites expressing QuasAr3, improvements were anomalously large, with a 170% increase in brightness between polarization parallel versus perpendicular to the dendrite. Signal/noise ratios of optically recorded action potentials were increased by up to 50% in neurites expressing QuasAr3. These results demonstrate that polarization control can be a facile means to enhance signals from fluorescent voltage indicators, particularly in thin neurites or in high-background environments.

SIGNIFICANCE Voltage imaging is a powerful technique for mapping the bioelectrical dynamics in electrically excitable cells, such as neurons and cardiomyocytes. However, fluorescent voltage indicators often give small signals that can be difficult to distinguish from noise. Voltage indicator molecules are oriented within cell membranes, so one can increase the fluorescence signal by exciting them with optimally polarized light. Here, we quantify the chromophore orientation in several fluorescent voltage indicators and demonstrate voltage imaging with improved sensitivity in neuron cell bodies and thin neurites by illuminating with optimal polarization.

INTRODUCTION

Electrical signaling is the central language of the nervous system, but historically membrane voltage has been difficult to measure. Patch-clamp measurements provide high sensitivity and time resolution but are laborious to perform, only report the voltage at a single point in space, and are particularly challenging in thin neurites (dendrites or axons). Optical measurements of membrane voltage are emerging as a powerful tool for mapping bioelectric effects in neurons (1–5), cardiomyocytes (6,7), and other electrically active cell types (8,9). Voltage imaging enables spatial mapping of bioelectrical signals and the possibility of probing mechanically inaccessible structures, but typically at the cost of reduced precision and reduced absolute accuracy compared to patch-clamp. Voltage indicators have been designed around protein (10,11), organic dye (12–14), and hybrid protein-dye (3,15) scaffolds. The development of improved voltage indicators is a subject of much ongoing research (16,17).

Despite recent advances, in many cases the signal/noise ratio (SNR) for voltage measurements remains low. The challenges are that the signals are brief (∼1 ms for a typical action potential), some reporters are very dim (e.g., those based on direct retinal fluorescence have ∼1% quantum yield), and fractional changes in fluorescence are often small (∼50% for an action potential for the most sensitive reporters). These challenges are compounded by the tissue environment, in which voltage-dependent signals are scattered by tissue and compete with background fluorescence. Methods for increasing the SNR would expand the capabilities of voltage imaging, potentially allowing for higher

Submitted July 21, 2021, and accepted for publication October 20, 2021.
*Correspondence: cohen@chemistry.harvard.edu
Editor: Baron Chanda.
https://doi.org/10.1016/j.bpj.2021.10.028

temporal resolution, recording from subcellular domains (e.g., dendrites), or recording deeper in tissue.

Improvements in signal quality could come equally from improved molecular reporters or from improved optical instrumentation. Compared with the efforts on the molecular reporters, less effort has gone into developing optical systems optimized for voltage imaging in tissue. The physical attributes of voltage indicators suggest that the optimal voltage-imaging system might be substantially different from systems designed for imaging reporters of other modalities (e.g., calcium).

All voltage indicators, regardless of mechanism, are physically localized to the cell membrane, a two-dimensional manifold embedded in a three-dimensional tissue. Useful signals only come from optical excitation targeted directly at the membrane; excitation either inside or outside of the target cell contributes to sample heating, background fluorescence, and phototoxicity, but not to signal. Efforts to localize two-photon (2P) (5,18) or one-photon (1P) (1,19,20) illumination to the membrane led to dramatic improvements to the SNR.

Membrane localization also raises the possibility of orientational order in voltage-reporting chromophores. Chromophores preferentially absorb light when the polarization of the excitation is aligned with the transition dipole between the ground and the electronically excited states. By optimizing this alignment at a patch of membrane, one might increase the in-focus fluorescence signal without affecting the background (in which chromophores are assumed to be randomly oriented) and thereby improve the SNR.

The degree of improvement in the fluorescence signal depends on the degree of orientational order in the membrane-bound chromophores and on the physical structure of the membranes of interest. In this article, we explore theoretically and experimentally the prospects for enhancing SNR by imaging with polarized optical excitation. We consider the organic dye indicator BeRST1 (12) and the protein-based indicators ASAP1 (11), QuasAr3 (1), ArcLight (21), Ace-mNeonGreen (22), and CAESR (23). Up to 73% enhancements in signal are observed for BeRST1 in cell bodies and 170% increases for QuasAr3 in thin neurites. These findings show that simple changes in optics could substantially enhance fluorescent voltage signals without increasing background.

MATERIALS AND METHODS

Expression of constructs in HEK293T cells

BeRST1 was a gift from Evan Miller (Berkeley); ASAP1 was a gift from Michael Lin (Stanford); Ace-mNeonGreen was a gift from Mark Schnitzer (Stanford); ArcLight was a gift from Vincent Pieribone (Yale). Addgene locations: ArcLight A242 in PCS2+, #36857; CAESR, #59172; FCK-ASAP1, #52519; QuasAr3 #107701.

Human embryonic kidney 293T (HEK293T) cells (CRL-11268; American Type Culture Collection, Manassas, VA) were cultured and transfected as described before (20). Briefly, cells were grown at 37°C, 5% CO_2, in Dulbecco's modified Eagle's medium (DMEM) supplemented with 10% fetal bovine serum and penicillin-streptomycin. Cells were tested negative for mycoplasma. Cells were transfected with CAESR, Quasar3, or ArcLight under the upstream cytomegalovirus (CMV) promoter of the FCK plasmid and with ASAP1 under the upstream CAG promoter of the pcDNA3.1/Puro-CAG backbone. 200–400 ng of plasmid DNA was transfected using Transit 293T (Mirus, Madison, WI) following the manufacturer's instructions. Cells were assayed 48 h after transfection. The day before recording, cells were replated onto Matrigel coated glass-bottom dishes (In Vitro Scientific, Mountain View, CA) at a density of ~10,000 cells/cm^2.

For voltage-sensitive dye imaging, HEK cells were incubated with BeRST1 as previously described (12). Cells were incubated in 1 μM BeRST1 in extracellular (XC) buffer for 15 min at 37°C and then washed to remove excess buffer.

Neural culture

All procedures involving animals were in accordance with the US National Institutes of Health Guide for the care and use of laboratory animals and were approved by the Institutional Animal Care and Use Committee at Harvard University.

Rat glial monolayers were prepared as described previously (24). Briefly, 10^6 dissociated hippocampal cells from P0 rat pups were plated on a 10 cm culture dish in glial medium (GM), composed of 15% fetal bovine serum (Life Technologies, Carlsbad, CA), 0.4% (w/v) D-glucose, 1% GlutaMAX (Life Technologies), and 1% penicillin/streptomycin (Life Technologies) in minimum essential medium (MEM, Life Technologies). When the dish reached confluence (1–2 weeks), cells were split using trypsin onto glass-bottom dishes (D35-20-1.5-N; In Vitro Scientific) coated with poly(D-lysine) and Matrigel (Becton Dickinson Biosciences, Franklin Lakes, NJ) at a density of 3500 cells/cm^2. After 3–6 days, glial monolayers were at or near confluence, and the medium was replaced by GM with 2 μM cytarabine (cytosine-β-arabinofuranoside; Sigma-Aldrich, St. Louis, MO) to prevent further glial growth. Dishes were maintained in GM with 2 μM cytarabine until use. Dishes were discarded if microglia or neurons were identified on the monolayers.

Hippocampal neurons from P0 rat pups were dissected and cultured in neurobasal-based medium (NBActiv4; BrainBits, Springfield, IL) at a density of 30,000–40,000 neurons/cm^2 on the pre-established glial monolayers. At 1 day in vitro (DIV), cytarabine was added to the neuronal culture medium at a final concentration of 2 μM to inhibit further glial growth (25). Neurons were transfected between 3 and 8 DIV via the calcium phosphate transfection method (26). Measurements on neurons were taken between 7 and 18 DIV.

Electrophysiology

All imaging and electrophysiology were performed in XC buffer containing 125 mM NaCl, 2.5 mM KCl, 3 mM $CaCl_2$, 1 mM $MgCl_2$, 15 mM HEPES, and 30 mM glucose (pH 7.3) and adjusted to 305–310 mOsm with sucrose. Patch-clamp measurements were performed with a HEKA EPC 800 patch-clamp amplifier. Filamented glass micropipettes (World Precision Instruments, Sarasota, FL) were pulled to a tip resistance of 5–10 MΩ and filled with internal solution containing 125 mM potassium gluconate, 8 mM NaCl, 0.6 mM $MgCl_2$, 0.1 mM $CaCl_2$, 1 mM EGTA, 10 mM HEPES, 4 mM Mg-ATP, and 0.4 mM Na-GTP (pH 7.3) and adjusted to 295 mOsm with sucrose. Pipettes were positioned with a Sutter MP285 manipulator (Sutter Instrument, Novato, CA). Whole-cell voltage-clamp and current-clamp signals were filtered at 3 kHz with the internal Bessel filter and digitized with a National Instruments PCIe 6259 board (Austin, TX).

Wide-field microscopy and polarization modulation

Whole-cell patch-clamp and fluorescence recordings were acquired on a home-built, combined 2P and inverted epifluorescence microscope

described before (20). The electrophysiology and optical measurements were synchronized via custom software written in LabView.

Fig. 2 *b* gives a schematic of the microscope pathway used for the wide-field experiments. We used 640 nm (QuasAr3, BeRST1) and 488 nm (all other indicators) Coherent Obis lasers (Santa Clara, CA) for excitation. The laser light was passed through a Gooch and Housego acousto-optical tunable filter (Ilminster, UK) and collimated and expanded using Thorlabs achromatic lenses (Newton, NJ) in flip mounts for varying magnification. The light was then passed through a liquid crystal variable retarder (LCVR) (LVR-200-IR1 LCVR for 640 nm excitation and LVR-200-VIS LCVR for 488 nm excitation; Meadowlark Optics, Frederick, CO) driven by a two-channel Tektronix arbitrary function generator. For 640 nm excitation, excitation light and fluorescence were separated using a Semrock FF660-Di02 dichroic mirror (Rochester, NY). For 488 nm excitation, excitation light and fluorescence were separated using a Semrock Di02-R488 dichroic mirror. Imaging was performed with an Olympus water immersion XPLN25XWMP2 objective (Center Valley, PA) with an NA of 1.05. Residual 640 nm laser light was rejected with a BLP01-664R-25 long-pass filter (Semrock). Residual 488 nm laser light was filtered with a BLP01-488R-25 (Semrock, Rochester, NY) long-pass filter. Imaging of HEK293T cells was performed on an Andor iXon X3 860 Ultra EMCCD (128 × 128 pixels, 24 μm pixel size; Belfast, Northern Ireland, UK) at a framerate of 10 Hz; imaging of action potentials in cultured neurons was performed on an Andor iXon X3 897 Ultra EMCCD (512 × 512 pixels, 16 μm pixel size) at a framerate of 1 kHz. All recordings were performed at room temperature.

Image processing

In small neurites, fluorescence F was very dim, so it was important to have an accurate calibration of the laser illumination profile and of any spurious signal sources. The two sources of spurious signal comprised counts when the laser was off (D, from dark counts, ambient light) and laser-dependent signal (L, bleedthrough and sample autofluorescence). The signal at each pixel was a sum $F + D + L$. Furthermore, we found that there were slight differences in illumination intensity and illumination profile for the two incident polarizations due to slight linear dichroism in the dichroic mirror in the microscope.

We recorded images of fluorescent cells (Fluor), calibration images of the dish and buffer without fluorescent cells (Cal) for each polarization, and a background image with the laser light off (Back). Background and calibration images were collected at the start of each recording session and after making any changes to camera settings. The background and calibration images were consistent throughout each recording session, provided camera settings remained constant. For each polarization, we calculated the following: final image = (Fluor − Cal)/(Cal − Back). This procedure ensured that the images reflected the underlying biological structure and not optical artifacts.

Regions of interest in Fig. S1 were selected for parts of neurites that were close to horizontal or vertical, without regard to magnitude of F or ΔF.

Signal processing

In the traces of Fig. 2, *b* and *c*, small offsets were subtracted to make the fluorescence-detected linear dichroism (FDLD) curves symmetric around zero. We attribute these small asymmetries to a slight polarization dependence of the transmission of the dichroic mirrors (27). The error bars on the fits (shown as *paler*, *transparent lines* in Fig. 2, *b* and *c*) were calculated using a bootstrap method that randomly sampled, with replacement line segments around the cell membranes to create resampled data sets of the original size. The uncertainties on the reported FDLD values are the standard deviations of the fits to each of the bootstrapped data sets. This nonparametric approach did not require assumptions about the underlying distribution of the data.

Theory

Brasselet and co-workers have presented a detailed study of the responses of chromophores in membranes to polarized 1P excitation (28). Here, we review the key results relevant to voltage imaging. When a fluorophore with excitation transition dipole $\boldsymbol{\mu}$ is excited by linearly polarized light with polarization vector $\mathbf{e}$, the fluorescence F is proportional to $|\boldsymbol{\mu} \cdot \mathbf{e}|^2$. Modulation of optical excitation by changes in linear polarization is called linear dichroism, and when the excitation is monitored via fluorescence, the phenomenon is called FDLD.

We assume that membrane-bound chromophores have free rotation about the surface normal but fixed orientation relative to the membrane plane. The population then has a cone-shaped distribution of transition dipoles, with the cone axis of symmetry along the membrane normal (Fig. 1 *a*). For high-NA objectives, the dipolar emission pattern is collected over enough angles that one can safely neglect the dependence of the collection efficiency on the orientation of $\boldsymbol{\mu}$ (29,30).

For illumination traveling orthogonal to the plane of the membrane, there can be no FDLD signal because of the azimuthal symmetry of the distribution of $\boldsymbol{\mu}$. However, when illuminating a cell from above, the membrane around the equator is illuminated edge on and offers the prospect of producing an FDLD signal. If the cone half-angle, θ_{cone}, of the distribution of transition dipole orientations is narrow, then the fluorescence is maximized when the polarization of the excitation is perpendicular to the membrane ($F_\perp$, Fig. 1 *b*). If θ_{cone} is wide, then the fluorescence is maximized when the polarization is in the plane of the membrane ($F_\parallel$, Fig. 1 *c*).

We define the FDLD by

$$\text{FDLD} \equiv \frac{(F_\parallel - F_\perp)}{\frac{1}{2}(F_\parallel + F_\perp)} \tag{1}$$

Assuming that the light is propagating entirely in the plane of the membrane, an average of the FDLD signal over all azimuthal chromophore orientations yields

$$\text{FDLD} = \frac{2 - 6\cos^2\theta_{cone}}{1 + \cos^2\theta_{\text{cone}}}, \tag{2}$$

The derivation is given in the Supporting materials and methods, Section 1.1. FDLD is between −200% (when $\theta_{\text{cone}} = 0°$) and 200% (when $\theta_{\text{cone}} = 90°$). There is no FDLD signal when $\theta_{\text{cone}} = 54.7°$, the so-called "magic angle." (31) An analogous calculation for 2P excitation is given in the Supporting materials and methods, Section 1.2

In an image of a roughly spherical cell under wide-field illumination, the fluorescence at the equatorial plane appears to be brighter than at the poles, a consequence of geometrical projection. To simulate this effect, we convolved a 10 μm diameter spherical shell (representative of a nominal cell membrane) with the point-spread functions of a series of objective lenses with different numerical apertures. Fig. 1 *d* shows the fluorescence enhancement at the equatorial membrane. This result demonstrates that one achieves more signal per input photon by targeting illumination to the equatorial periphery of the cell rather than flood illuminating the whole cell. One should then either 1) select the polarization as a function of azimuth around the cell equator to maximize the FDLD signal or 2) use illumination of a single polarization and target the excitation to the azimuthal angles at which the polarization is most efficient at exciting the reporter.

The shot-noise-limited SNR in a voltage-imaging experiment is

$$\text{SNR} = \frac{\Delta F^{(V)}}{\sqrt{F + B}}, \tag{3}$$

where $\Delta F^{(V)}$ is the change in fluorescence associated with the electrical event of interest, F is the baseline fluorescence of the reporter, and B is the background fluorescence, all expressed in photon counts. The

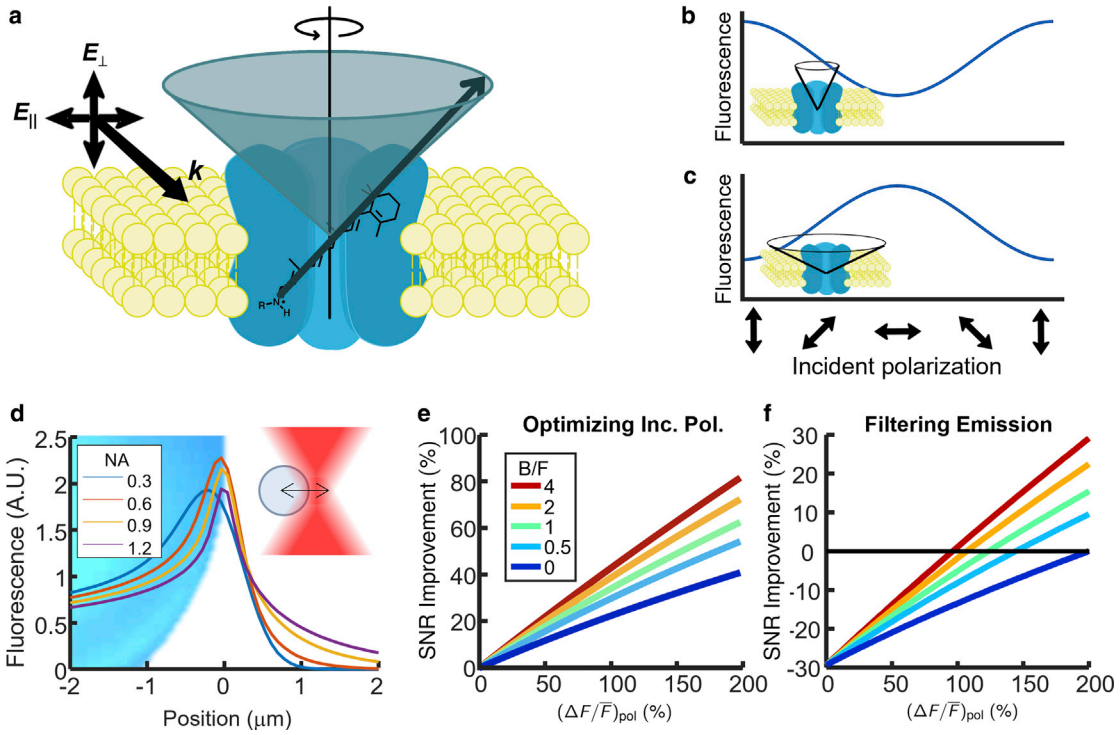

FIGURE 1 Polarized excitation can enhance signal from membrane-bound indicators. (*a*) Geometry of a voltage-indicating chromophore in a membrane. An ensemble of chromophores has a cone-shaped distribution of transition dipoles. (*b*) When light propagates in the plane of the membrane, the efficiency of fluorescence excitation depends on the polarization. Out-of-plane polarization favors excitation for chromophores with a narrow cone angle, and (*c*) in-plane polarization favors excitation for chromophores with a wide cone angle. (*d*) Total fluorescence emission from a 10 μm diameter spherical shell illuminated with an unpolarized diffraction-limited Gaussian beam. Total fluorescence is relatively insensitive to illumination NA but is substantially enhanced at the equator of the sphere. (*e*) Theoretical shot-noise-limited SNR improvement from optimizing the polarization of the incident light (compared with the expectation value of the SNR under a random linear polarization). (*f*) Theoretical SNR improvement from filtering the emission by polarization. *B*/*F* is the background fluorescence divided by the fluorescence from the indicator. Legend applies to (*e*) and (*f*). To see this figure in color, go online.

denominator represents the shot noise, and the numerator represents the voltage-dependent signal. Favorable polarization alignment enhances $\Delta F^{(V)}$ and F proportionally, without affecting B. Fig. 1 *e* plots the predicted enhancement in SNR from favorable polarization versus random polarization as a function of the amplitude of the FDLD signal, showing the possibility for nearly twofold enhancement in SNR (Supporting materials and methods, Section 2.1).

In principle, one might achieve further enhancement of signal/background ratio by passing the emission through an appropriately aligned polarizer, too. The background fluorescence is (presumably) unpolarized, whereas the signal fluorescence retains some polarization, both because of selection of oriented chromophores by the polarized excitation and by polarized emission from the inhomogeneous distribution of chromophore orientations in the membrane. A polarizer in the emission path could, in principle, increase the signal/background ratio by passing the polarized in-focus emission while rejecting half the unpolarized background. Fig. 1 *f* shows that the resulting enhancement in SNR is predicted to be small and often negative, so this approach was not considered further (Supporting materials and methods, Section 2.2).

RESULTS

FDLD in HEK cells

We developed an optical system to illuminate a sample with collimated laser illumination at a variety of wavelengths, with synchronized polarization control and image acquisition (Fig. 2 *a*, Materials and methods). We began by measuring the FDLD signals of BeRST1 ($N = 2$ cells), ASAP1 ($N = 4$ cells), QuasAr3 ($N = 2$ cells), ArcLight ($N = 3$ cells), Ace-mNeonGreen ($N = 3$ cells), and CAESR ($N = 4$ cells) in HEK cells. For each cell, we recorded widefield epifluorescence images while alternating the polarization of the incident light between horizontal and vertical linear polarizations. We averaged the frames corresponding to each condition and calculated the FDLD signal pixel by pixel.

We created a trace of the cell membranes by manually defining the vertices of a series of line segments around the periphery of each cell. We extracted the FDLD signal as a function of position along the trace and calculated the membrane surface normal for each line segment. We binned the sampled FDLD values by line segment, combined the data from all cells expressing each indicator, and fitted a sinusoidal curve for FDLD as a function of membrane surface normal (Materials and methods and Supporting materials and methods). The process of mapping the orientation-dependent FDLD signal is illustrated for a single ASAP-expressing cell in Fig. 2 *b*.

Fig. 2 *c* shows the results for each voltage indicator. The FDLD values on each panel use the sign convention from Eq. 1. Rearranging Eq. 1 shows that the ratio of fluorescence with polarization optimal versus orthogonal is given by

$$\frac{F_{\text{optimal}}}{F_{\text{orthog}}} = \frac{2 + |\text{FDLD}|}{2 - |\text{FDLD}|} \tag{4}$$

This ratio is BeRST1 1.73 ± 0.056, ASAP1 1.22 ± 0.009, QuasAr3 1.14 ± 0.009, ArcLight 1.12 ± 0.009, Ace-mNeonGreen 1.046 ± 0.006, and CAESR 1 ± 0.003. The voltage-sensitive dye BeRST1 and the protein-based sensor ASAP1 had the FDLD signals with the largest magnitudes, though they were of opposite sign, suggesting that the BeRST1 chromophore has an orientation close to the plane of the membrane, whereas the ASAP1 chromophore is approximately perpendicular to the membrane. Indeed, the molecular structure of BeRST1 has a "T" shape, with a molecular wire penetrating the membrane and the chromophore in the membrane plane (12).

The QuasAr3 reporter also showed a substantial FDLD signal, a consequence of the fixed orientation of the retinal chromophore relative to the protein scaffold. The two FRET-based protein reporters, Ace-mNeonGreen and CAESR, showed small FDLD signals, presumably a consequence of tumbling of the fluorescent protein that was tethered loosely to the membrane. The values of the FDLD signals corresponded to the following ensemble-averaged cone angles: BeRST1 62 ± 4°, ASAP1 52 ± 0.1°, QuasAr3 56.4 ± 0.1°, ArcLight 56.3 ± 0.1°, Ace-mNeonGreen 55.4 ± 0.08°, and CAESR 54.7 ± 0.04°, though the values for Ace-mNeonGreen and CAESR more likely reflect orientational averaging rather than a distribution peaked around a specific cone angle.

We combined patch-clamp electrophysiology and polarization-resolved fluorescence imaging to record the mean fluorescence and FDLD as a function of membrane potential. All the reporters showed voltage-dependent changes in mean fluorescence consistent with literature reports. The polarization-dependent enhancements in baseline fluorescence, F, and in voltage-dependent changes in fluorescence, $\Delta F^{(V)}$, were proportional, so the nominal sensitivity, $\Delta F^{(V)}/F$, did not depend on polarization. These findings imply that voltage-induced changes in the ensemble-average cone angle were below our detection sensitivity. Although polarization did not affect $\Delta F^{(V)}/F$, the increase in absolute brightness upon optimal polarization led to an improvement in the shot-noise-limited SNR via Eq. 3. Previous work reported a voltage-dependent 2P FDLD signal in ArcLight (32). Our failure to observe this effect is likely due to the lower orientational sensitivity of 1P vs. 2P linear dichroism measurements (33).

Axons and dendrites

Next, we considered FDLD measurements in thin neurites (axons or dendrites), in which voltage imaging is particularly challenging because of the small membrane surface areas. We calculated the predicted dependence of the FDLD signal on chromophore cone angle in the cylindrical geometry of a slender neurite. We assumed that the fluorescence was averaged over the circumference of the neurite, i.e., that the transverse structure of the neurite was not

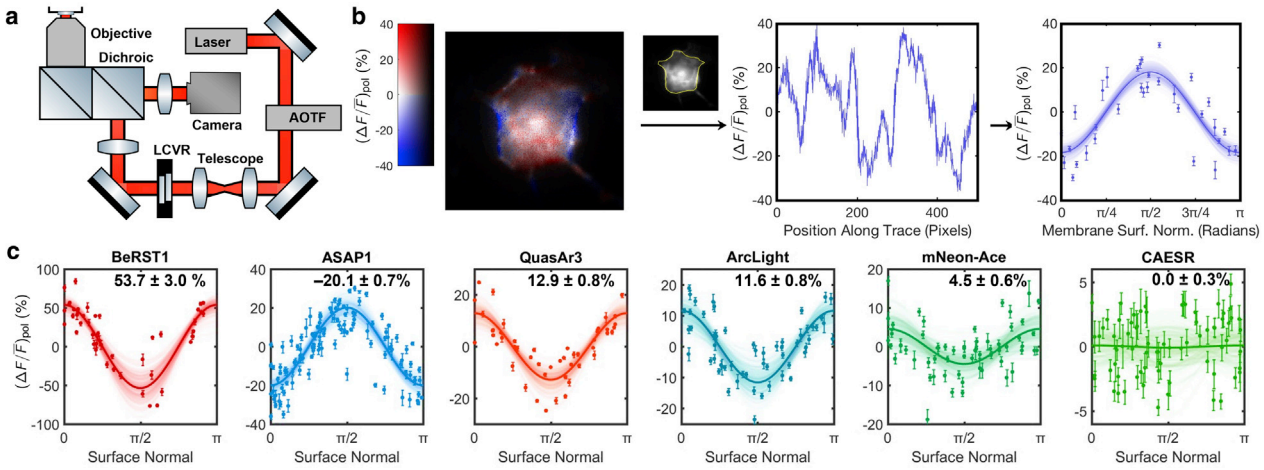

FIGURE 2 Fluorescence-detected linear dichroism in voltage-indicating chromophores. (*a*) Microscope used for wide-field imaging experiments. Details of the setup are in Materials and methods. The acousto-optical tunable filter (AOTF) modulated the illumination intensity, and the liquid crystal variable retarder (LCVR) provided polarization control. (*b*) Steps for measuring linear dichroism in cells. Fluorescence images were acquired under orthogonal polarizations. The FDLD signal was extracted along the perimeter of the cell and then mapped as a function of the direction of the membrane surface normal. (*c*) Linear dichroism data from HEK cells labeled with BeRST1, ASAP1, QuasAr3, ArcLight, Ace-mNeonGreen, and CAESR. Colors correspond to approximate absorption peaks for each indicator. Each point corresponds to a line segment from a trace of a cell perimeter, and its error bar represents the standard error in the average FDLD for the pixels in that line segment. Data from all imaged cells are combined in (*c*). To see this figure in color, go online.

resolved. The optical excitation strength, $|\boldsymbol{\mu} \cdot \mathbf{e}|^2$, was a function of three angles: the cone half-angle θ_{cone} for the distribution of chromophore orientations relative to the surface normal, the azimuthal angle ϕ_1 about the surface normal, and an azimuthal angle ϕ_2 about the axis of the neurite. This model and these angles are illustrated in Fig. 3 *a*.

The relationship between the θ_{cone} and the polarization anisotropy is

$$\text{FDLD}_{\text{neurite}} = \frac{2 - 6\cos^2\theta_{\text{cone}}}{3 - \cos^2\theta_{\text{cone}}} \tag{5}$$

The derivation is given in the Supporting materials and methods, Section 1.3. Equation 5 predicts that FDLD has a lower limit of −200% in the case of $\theta_{\text{cone}} = 0°$ and an upper limit of 66.7% in the case of $\theta_{\text{cone}} = 90°$. This result differs from the calculations for a flat section of membrane in which the bounds were −200 and 200%. This difference arises because of contributions in the neurites from the top and bottom surfaces. A surface perpendicular to the direction of light propagation has zero FDLD, but for $\theta_{\text{cone}} > 0°$, the surface nonetheless contributes fluorescence. Mixing the fluorescence from the top and bottom surfaces with the fluorescence from the edges of the neurite leads to a decrease in the maximal FDLD signal when θ_{cone} approaches 90°.

We measured linear dichroism in neurites of cultured neurons using the three indicators that exhibited the greatest FDLD signals: BeRST1, ASAP1, and QuasAr3. Fig. 3, *c–e* gives example fields of view for each indicator. We collected 9–27 fields of view for each indicator (most of which contained multiple neurites). We looked only at

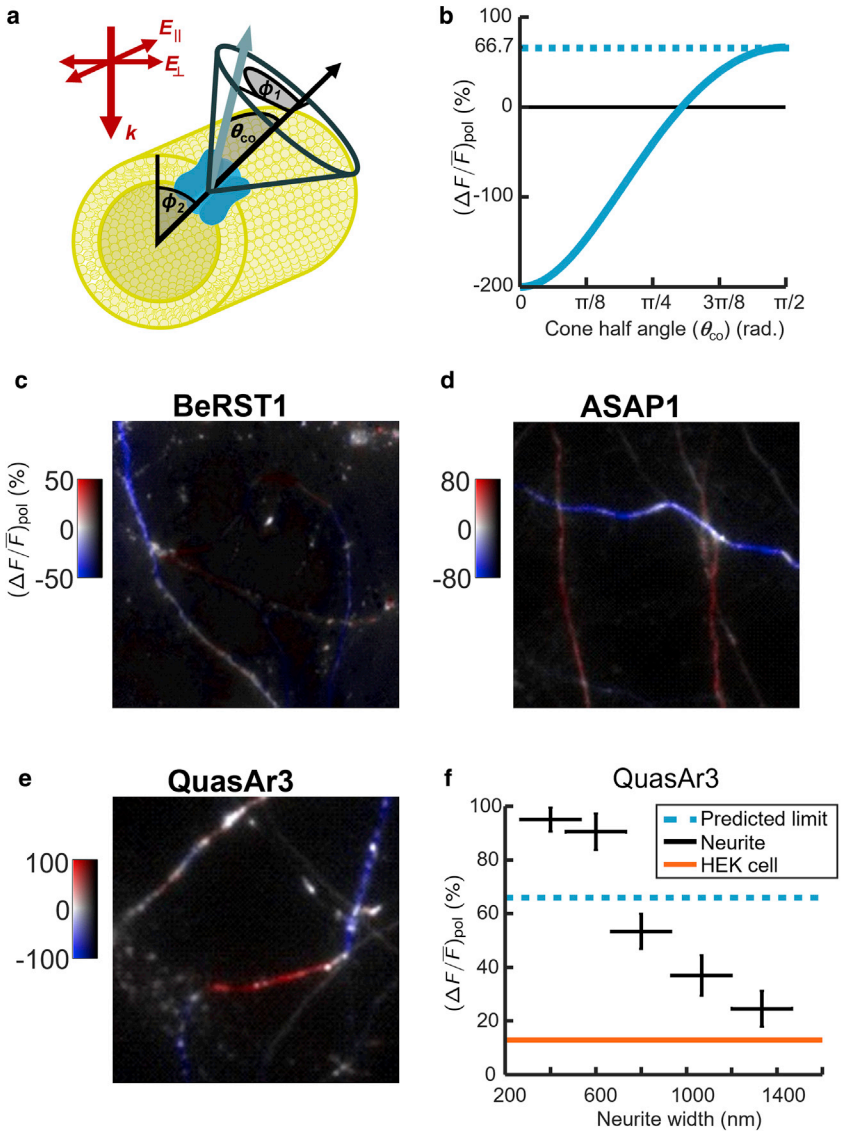

FIGURE 3 Polarized excitation enhances voltage indicator fluorescence in neurites. (*a*) Geometry of a neurite showing the distribution of chromophore orientations. FDLD signals are calculated by averaging over ϕ_1 and ϕ_2. (*b*) FDLD signal as a function of chromophore cone angle, assuming that photons are binned across the diameter of the neurite. FDLD images were acquired for neurons labeled with (*c*) BeRST1, (*d*) ASAP1, and (*e*) QuasAr3. (*f*) In neurites expressing QuasAr3, the FDLD signal was enhanced in thinner neurites relative to thicker ones. The orange line represents the FDLD signal measured in cell bodies. The blue dashed line represents the theoretical maximal FDLD signal, assuming isotropic in-plane chromophore orientations. Neurites were manually sorted by width into five bins ($N = 41$ neurites). The smallest bin corresponded to neurites with widths below the resolving power of the microscope. The remaining bins corresponded to neurites with widths of ~2, 3, 4, and 5 pixels in the recorded images. Error bars represent the width of the bins and the standard error of the mean FDLD for the neurites in each bin. To see this figure in color, go online.

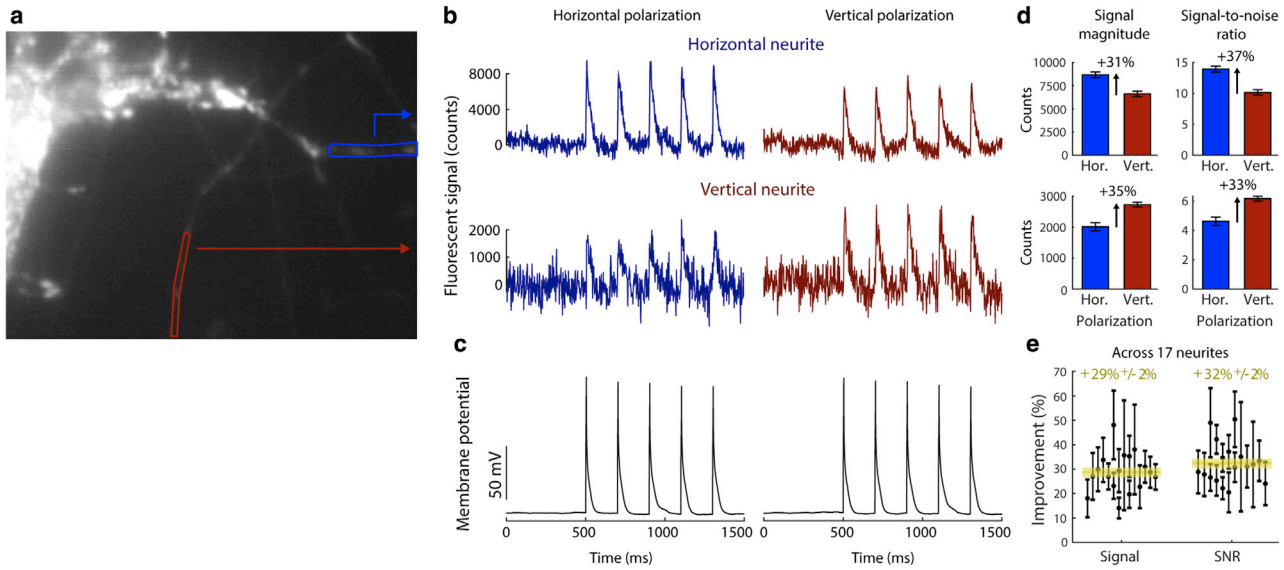

FIGURE 4 Polarized excitation enhances voltage-dependent signals in neurites. (*a*) Example neuron with regions indicating horizontally and vertically aligned neurites. Current injection via a patch pipette (4 ms, 400 pA, 5 Hz) triggered action potentials. (*b*) Fluorescence intensity traces averaged over nine trials with each polarization. (*c*) Membrane potential averaged over nine trials. (*d*) Signal magnitude and signal/noise ratios under horizontal and vertical polarizations for the neuron in (*a*)–(*c*). Background and noise were calculated as the mean and standard deviation of the fluorescence during the 500 ms before the first current pulse. The peak fluorescence in the 25 ms after the current pulse was used as the signal. Error bars represent the standard error across the five action potentials. (*e*) Signal magnitude and signal/noise ratio improvements for each of 17 neurites from six cells shown in black with mean improvements in yellow. To see this figure in color, go online.

nearly vertical and nearly horizontal neurites and sorted our observations by neurite width. In the thinnest neurites (i.e., those with diameters near or below the diffraction limit), we observed FDLD values BeRST1 30.9 ± 0.7% ($N = 14$), ASAP1 −59.1 ± 0.4% ($N = 21$), and QuasAr3 92.5 ± 1.2% ($N = 19$). These FDLD values correspond to fluorescence ratios $F_{optimal}/F_{orthog}$: BeRST1 1.37 ± 0.01, ASAP1 1.84 ± 0.008, and QuasAr3 2.72 ± 0.04, i.e., there was a 172% enhancement in the QuasAr3 signal by optimizing the polarization.

The anticipated FDLD values in the neurites can be obtained by reference to Fig. 3 *b* and the cone angles extracted from the measurements on the HEK cells. Based on the HEK cell measurements, one would anticipate FDLD values in neurites to be 24 ± 12% for BeRST1, −10.5 ± 0.4% for ASAP1, and 6.0 ± 0.4% for QuasAr3. For QuasAr3 and ASAP1, the measured values are much larger than the predictions, whereas for BeRST1, the predicted and measured values were similar. In the somas of the neurons, we observed FDLD values similar to those from HEK cells, indicating that the anomalously large FDLD values in neurites were not due to a neuron-specific change in θ_{cone}.

The data for QuasAr3 were particularly striking because these results showed FDLD values in the thinnest neurites (92.5 ± 1.2%) that exceeded the maximal theoretical value, 66.7%, corresponding to $\theta_{cone} = 90°$. Although the reason for this discrepancy is not known, we speculate that it may reflect an inhomogeneous distribution of azimuthal orientations (ϕ_1) in the membrane. The strong curvature around the neurite axis could break the azimuthal symmetry, favoring some values of ϕ_1 over others (e.g., if the molecule itself lacks cylindrical symmetry in the membrane plane). We are not aware of examples of curvature-induced orientational order in proteins, so this idea at present remains speculation. The FDLD for ASAP1 in neurites also exceeded the anticipated value based on θ_{cone} measured in HEK cells, but it was within the theoretically allowed range. The FDLD for the small-molecule dye BeRST1 was as expected.

Functional recordings in neurons

To assess whether polarized illumination could improve the SNR of voltage imaging, we made optical recordings from neurites of cultured neurons. Cultured neurons were transfected with QuasAr3 and subjected to simultaneous patch-clamp electrophysiology and high-speed fluorescence imaging. Action potentials were induced via current injection, and voltage and fluorescence responses were recorded simultaneously. We interleaved trials with vertical and horizontal polarized illumination.

Fig. 4 shows a typical example. Fluorescence signals from the neurites showed clear polarization dependence. The degree of signal enhancement varied considerably, depending upon the diameter, orientation, and smoothness of the neurite. From neurites that were well aligned with the vertical or horizontal axes, appeared to be relatively smooth, and gave a reliable fluorescent response to action potentials, the mean enhancement in signal between the optimal and

orthogonal polarizations was 29 ± 2%, with a range from 14 to 48% ($N = 17$ neurites, 6 neurons). The mean SNR enhancement was 32 ± 2% with a range from 20 to 50%. In some instances, the improvement was such that fluorescent signals were visually discernable under the optimal polarization, but not the orthogonal polarization (Fig. S1). Considering that this enhancement only required minimal changes in the experimental setup and did not require any changes to the molecular tools or mode of gene expression, we suggest that polarized illumination could be a valuable addition to voltage-imaging efforts, particularly in thin neurites.

DISCUSSION

The polarization-dependent effects observed here are modest for measurements of cell bodies (~36% improvement in brightness for optimally polarized versus unpolarized illumination of BeRST1) but substantially larger for very thin neurites (~85% improvement for optimally polarized versus unpolarized illumination of QuasAr3). These values reflect intrinsic properties of the different reporters, and further enhancements in FDLD signals would require new protein or small-molecule scaffolds. Although the enhancements are modest, achieving comparable increases in SNR via protein engineering is often a major undertaking. Historically, advances in voltage imaging have come from concatenating many incremental improvements in SNR, of which polarization control can be a useful contributor (17).

Implementing polarization control in an existing voltage-imaging setup is comparatively straightforward. However, one should be attentive to the fact that most dielectric mirrors and dichroic mirrors have strong linear birefringence, so linearly polarized light introduced into a microscope optical path may no longer be linearly polarized at the sample. Because most lasers emit linearly polarized light, the illumination in many voltage-imaging setups may be in a state of arbitrary elliptical polarization, which could lead to substantial variations in extracted signals depending upon the fortuitous alignment of membranes with the major axis of polarization. Such fortuitous alignments would not occur with unpolarized illumination (e.g., from a light-emitting diode). Supporting materials and methods, Section 2.1 gives an expression for the enhancement of optimally polarized relative to unpolarized illumination. Enhancement over unpolarized illumination can be determined from the values reported here comparing different pure linear polarization states. Optimal linear polarization can always produce better SNR than can unpolarized illumination.

In tissues in which background signal comes from out-of-focus reporter molecules, individual out-of-focus membranes may show an FDLD signal. However, the background is typically composed of an average over many membranes. Provided that the membranes are, on average, isotropically oriented, the background will not have an FDLD signal. If imaging in fiber tracts or other oriented tissues, then the incident polarization may need to be adjusted to minimize the contribution from out-of-focus fluorescence.

The practical implications of the improvements reported here will depend on the experimental context. Dendritic voltage imaging in acute brain slices and in vivo may be an area in which polarization control is particularly useful because signals are small, background is large, and FDLD in thin neurites is particularly enhanced. Efforts are underway to apply polarized light voltage imaging to this problem. Other potential applications include improved estimates of subthreshold or action potential waveforms and voltage imaging deeper in scattering tissue.

Depending on the expression level of the reporter, the size and depth of the target structure, and the optical properties of the surrounding tissue, the ratio of in-focus signal (F) to out-of-focus background (B) can range from very small to very large. When trying to image small structures or at depth, the background becomes high compared to the signal, so SNR $\approx \Delta F/\sqrt{B}$. Much effort has been devoted to increasing the brightness of microbial rhodopsin-based voltage sensors. If the background B is due to out-of-focus reporter molecules, then increases in molecular brightness or expression level increase F and B proportionally. Equation 3 shows that increasing the brightness by a factor x only increases the SNR by a factor of $\sqrt{x}$. In contrast, increasing the in-focus signals F and ΔF by an amount x without affecting the out-of-focus background B (e.g., by tuning incident polarization) increases SNR by a factor of x in the high-background limit. Thus, in the high-background limit, a twofold increase in in-focus brightness is equivalent, from an SNR perspective, to a fourfold increase in reporter brightness. These scaling arguments show that tuning incident polarization can be a useful means to enhance small voltage-imaging signals.

Considerable effort is being dedicated to developing 2P excitable voltage indicators with the hope that these tools will enable deeper imaging in intact tissue. The polarization sensitivity for 2P excitation is proportional to $|\boldsymbol{\mu} \cdot \mathbf{e}|^4$, leading to a much steeper polarization dependence than for 1P excitation (34). Indeed, polarized 2P excitation was previously used to probe the mechanism of a voltage-sensitive protein, ArcLight (32). In view of the strong polarization dependence, it will be important to control the polarization of the excitation, particularly when performing 2P voltage imaging in thin axons and dendrites.

Membrane-bound reporters are being developed for other modalities beside voltage, including, e.g., glutamate (35), gamma-aminobutyric acid (GABA) (36), acetylcholine (37), dopamine (38), and serotonin (39). The degree of chromophore orientation in these other molecules is not known.

We suggest that these other probes merit polarization analysis to determine whether signal levels can be enhanced through polarization control.

SUPPORTING MATERIAL

Supporting material can be found online at https://doi.org/10.1016/j.bpj.2021.10.028.

AUTHOR CONTRIBUTIONS

All authors designed the research. W.B., D.B., and S.K. built the apparatus. W.B. and D.B. performed the experiments and data analysis. W.B., D.B., and A.E.C. wrote the manuscript.

ACKNOWLEDGMENTS

We thank K. Williams for technical assistance with molecular biology and M. Lee for technical assistance with cell culture.

This work was supported by National Institutes of Health grant R01-MH117042 and the Howard Hughes Medical Institute. D.B. acknowledges support by a Dutch Research Council (NWO) Start-up Grant (740.018.018) and European Research Council (ERC) Starting Grant (850818—MULTI-VIsion). A.E.C. is a co-founder of Q-State Biosciences.

REFERENCES

1. Adam, Y., J. J. Kim, …, A. E. Cohen. 2019. Voltage imaging and optogenetics reveal behaviour-dependent changes in hippocampal dynamics. *Nature.* 569:413–417.
2. Piatkevich, K. D., S. Bensussen, …, X. Han. 2019. Population imaging of neural activity in awake behaving mice. *Nature.* 574:413–417.
3. Abdelfattah, A. S., T. Kawashima, …, E. R. Schreiter. 2019. Bright and photostable chemigenetic indicators for extended in vivo voltage imaging. *Science.* 365:699–704.
4. Kannan, M., G. Vasan, …, V. A. Pieribone. 2018. Fast, in vivo voltage imaging using a red fluorescent indicator. *Nat. Methods.* 15:1108–1116.
5. Villette, V., M. Chavarha, …, M. Z. Lin. 2019. Ultrafast two-photon imaging of a high-gain voltage indicator in awake behaving mice. *Cell.* 179:1590–1608.e23.
6. Klimas, A., C. M. Ambrosi, …, E. Entcheva. 2016. OptoDyCE as an automated system for high-throughput all-optical dynamic cardiac electrophysiology. *Nat. Commun.* 7:11542.
7. Dempsey, G. T., K. W. Chaudhary, …, J. M. Kralj. 2016. Cardiotoxicity screening with simultaneous optogenetic pacing, voltage imaging and calcium imaging. *J. Pharmacol. Toxicol. Methods.* 81:240–250.
8. McNamara, H. M., S. Dodson, …, A. E. Cohen. 2018. Geometry-dependent arrhythmias in electrically excitable tissues. *Cell Syst.* 7:359–370.e6.
9. Zhang, H., E. Reichert, and A. E. Cohen. 2016. Optical electrophysiology for probing function and pharmacology of voltage-gated ion channels. *eLife.* 5:e15202.
10. Hochbaum, D. R., Y. Zhao, …, A. E. Cohen. 2014. All-optical electrophysiology in mammalian neurons using engineered microbial rhodopsins. *Nat. Methods.* 11:825–833.
11. St-Pierre, F., J. D. Marshall, …, M. Z. Lin. 2014. High-fidelity optical reporting of neuronal electrical activity with an ultrafast fluorescent voltage sensor. *Nat. Neurosci.* 17:884–889.
12. Huang, Y. L., A. S. Walker, and E. W. Miller. 2015. A photostable silicon rhodamine platform for optical voltage sensing. *J. Am. Chem. Soc.* 137:10767–10776.
13. Miller, E. W., J. Y. Lin, …, R. Y. Tsien. 2012. Optically monitoring voltage in neurons by photo-induced electron transfer through molecular wires. *Proc. Natl. Acad. Sci. USA.* 109:2114–2119.
14. Yan, P., C. D. Acker, and L. M. Loew. 2018. Tethered bichromophoric fluorophore quencher voltage sensitive dyes. *ACS Sens.* 3:2621–2628.
15. Ghitani, N., P. O. Bayguinov, …, M. B. Jackson. 2015. Single-trial imaging of spikes and synaptic potentials in single neurons in brain slices with genetically encoded hybrid voltage sensor. *J. Neurophysiol.* 113:1249–1259.
16. Xu, Y., P. Zou, and A. E. Cohen. 2017. Voltage imaging with genetically encoded indicators. *Curr. Opin. Chem. Biol.* 39:1–10.
17. Adam, Y. 2021. All-optical electrophysiology in behaving animals. *J. Neurosci. Methods.* 353:109101.
18. Chamberland, S., H. H. Yang, …, F. St-Pierre. 2017. Fast two-photon imaging of subcellular voltage dynamics in neuronal tissue with genetically encoded indicators. *eLife.* 6:e25690.
19. Fan, L. Z., S. Kheifets, …, A. E. Cohen. 2020. All-optical electrophysiology reveals the role of lateral inhibition in sensory processing in cortical layer 1. *Cell.* 180:521–535.e18.
20. Chien, M. P., D. Brinks, …, A. E. Cohen. 2021. Photoactivated voltage imaging in tissue with an archaerhodopsin-derived reporter. *Sci. Adv.* 7:eabe3216.
21. Cao, G., J. Platisa, …, M. N. Nitabach. 2013. Genetically targeted optical electrophysiology in intact neural circuits. *Cell.* 154:904–913.
22. Gong, Y., C. Huang, …, M. J. Schnitzer. 2015. High-speed recording of neural spikes in awake mice and flies with a fluorescent voltage sensor. *Science.* 350:1361–1366.
23. Brinks, D., A. J. Klein, and A. E. Cohen. 2015. Two-photon lifetime imaging of voltage indicating proteins as a probe of absolute membrane voltage. *Biophys. J.* 109:914–921.
24. McCarthy, K. D., and J. de Vellis. 1980. Preparation of separate astroglial and oligodendroglial cell cultures from rat cerebral tissue. *J. Cell Biol.* 85:890–902.
25. Chen, G., N. C. Harata, and R. W. Tsien. 2004. Paired-pulse depression of unitary quantal amplitude at single hippocampal synapses. *Proc. Natl. Acad. Sci. USA.* 101:1063–1068.
26. Jiang, M., and G. Chen. 2006. High Ca2+-phosphate transfection efficiency in low-density neuronal cultures. *Nat. Protoc.* 1:695–700.
27. Tang, Y., T. A. Cook, and A. E. Cohen. 2009. Limits on fluorescence detected circular dichroism of single helicene molecules. *J. Phys. Chem. A.* 113:6213–6216.
28. Kress, A., X. Wang, …, S. Brasselet. 2013. Mapping the local organization of cell membranes using excitation-polarization-resolved confocal fluorescence microscopy. *Biophys. J.* 105:127–136.
29. Böhmer, M., and J. Enderlein. 2003. Orientation imaging of single molecules by wide-field epifluorescence microscopy. *J. Opt. Soc. Am. B.* 20:554–559.
30. Nevskyi, O., R. Tsukanov, …, J. Enderlein. 2020. Fluorescence polarization filtering for accurate single molecule localization. *APL Photonics.* 5:061302.
31. Fisz, J. J. 2007. Fluorescence polarization spectroscopy at combined high-aperture excitation and detection: application to one-photon-excitation fluorescence microscopy. *J. Phys. Chem. A.* 111:8606–8621.
32. Han, Z., L. Jin, …, V. A. Pieribone. 2014. Mechanistic studies of the genetically encoded fluorescent protein voltage probe ArcLight. *PLoS One.* 9:e113873.
33. Lazar, J., A. Bondar, …, S. J. Firestein. 2011. Two-photon polarization microscopy reveals protein structure and function. *Nat. Methods.* 8:684–690.

34. Gasecka, A., T. J. Han, …, S. Brasselet. 2009. Quantitative imaging of molecular order in lipid membranes using two-photon fluorescence polarimetry. *Biophys. J.* 97:2854–2862.

35. Marvin, J. S., B. G. Borghuis, …, L. L. Looger. 2013. An optimized fluorescent probe for visualizing glutamate neurotransmission. *Nat. Methods.* 10:162–170.

36. Marvin, J. S., Y. Shimoda, …, L. L. Looger. 2019. A genetically encoded fluorescent sensor for in vivo imaging of GABA. *Nat. Methods.* 16:763–770.

37. Jing, M., P. Zhang, …, Y. Li. 2018. A genetically encoded fluorescent acetylcholine indicator for in vitro and in vivo studies. *Nat. Biotechnol.* 36:726–737.

38. Patriarchi, T., J. R. Cho, …, L. Tian. 2018. Ultrafast neuronal imaging of dopamine dynamics with designed genetically encoded sensors. *Science.* 360:eaat4422.

39. Unger, E. K., J. P. Keller, …, L. Tian. 2020. Directed evolution of a selective and sensitive serotonin sensor via machine learning. *Cell.* 183:1986–2002.e26.